PNAS
www.pnas.org

Supplementary Information for

Spontaneous driving forces give rise to protein-RNA condensates with coexisting phases and complex material properties

Steven Boeynaems*, Alex S. Holehouse, Venera Weinhardt, Denes Kovacs, Joris Van Lindt, Carolyn Larabell, Ludo Van Den Bosch, Rhiju Das, Peter S. Tompa, Rohit V. Pappu*, and Aaron D. Gitler*

*Corresponding authors:
Steven Boeynaems
E-mail: sboeynae@stanford.edu

Rohit V. Pappu
E-mail: pappu@wustl.edu

Aaron D. Gitler
E-mail: agitler@stanford.edu

This PDF file includes:

www.pnas.org/cgi/doi/10.1073/pnas.1821038116

Polyanions, synthetic peptides and recombinant proteins

Poly-rU, poly-rC, poly-rG, poly-rA, total yeast RNA, heparin, chondroitin and polyphosphate were purchased from Sigma-Aldrich. Albumin was purchased from Rockland, Inc. Microtubules were purchased from Cytoskeleton Inc. rRNA was purchased from Bio-World. Salmon sperm DNA (ssDNA) was purchased from Ambion (Thermo Scientific). All polyanions were dissolved in milli-Q water and stored at −20°C. We purchased chemically synthesized peptides from Pepscan (Lelystad, Netherlands). Peptides were dissolved in milli-Q water and stored at −20°C. FUS and hnRNPA2 LC domains were expressed in E. coli and purified as described previously (1, 2). Peptides and proteins were fluorescently labeled using Alexa Fluor Labeling Kits (Thermo Scientific). Fluorescent RNA oligomers were synthesized by IDT. Fluorescent peptides or RNA oligomers were spiked in at 200 nM and 100 nM respectively as final concentrations. Fluorescent low complexity domains (LCDs) were spiked in at 1 μM.

Induction of phase separation

Polyanions were diluted to 1 μg/μL in 100 mM K_2HPO_4 / KH_2PO_4 buffer at pH 7. Peptides were added at 250 μM concentrations. All reactions were carried out at room temperature (≈ 25˚C), unless indicated otherwise. For fluorescence microscopy and FRAP analyses, labeled peptides were spiked in at 1 μM. For partitioning experiments, probe molecules were spiked in at 100 nM. For the generation of pure RNA liquid droplets, homopolymeric RNAs were diluted to 2 μg/μL in 1x PBS buffer with 30% PEG and 10 mM $MgCl_2$ at pH 7.

Bio-layer interferometry (BLI)

Homopolymeric RNAs (Sigma) were N-terminally biotinylated (ThermoFisher, 20160) and immobilized on super streptavidin biosensors (ForteBio, 18-5065) in Octet RED96 device (FortBio), at 70 μg/mL concentration for 80s at RT. The following average response values were reached at the sensor loading step, poly-rU: 0.20 ± 0.02 nm, poly-rA: 0.22 +/- 0.03 nm, poly-rC: 0.19 ± 0.03 nm, poly-rG: 0.23 ± 0.01 nm. Sensors were subsequently blocked in 0.01mg/ml biocytine for 60s and washed. After recording baseline in fresh buffer, association was performed in increasing concentration of PR30 (0 nM, 10 nM, 100 nM, 250 nM, 600 nM, 1 μM) for 400 s and dissociation was followed in the same well where baseline was recorded for 800s. Interferograms were background corrected with traces recorded on biocytine blocked sensors, immersed into the same PR30 samples. Every component throughout the experiment was dissolved in 1x kinetic buffer (ForteBio), supplemented with PBS, according to the manufacturer's guidelines. Individual concentration curves were fitted with a ForteBio analysis software, using 1:1 kinetics model, and values extracted for individual experiments. Saturation values of association phase were then transferred to GraphPad Prism 7.02, plotted in the function of PR30 concentrations.

Fluorescence recovery after photobleaching (FRAP)

Details of the protocol were as previously published (3). In brief, fluorescent droplets were incubated in plastic Cell Counter slides (Bio-Rad) at room temperature. Chambers were sealed using nail varnish to prevent evaporation during aging. To generate large droplets and / or large multilayered condensates, samples were briefly centrifuged for 30 s at 1200 rpm in a bench top centrifuge 5810R (Eppendorf). Fluorescence recovery after bleaching was monitored using Zen

software on a Zeiss LSM 780 Meta NLO confocal microscope equipped with a 20x long-range objective. For intra-droplet FRAP, a circular area of 1 μM radius was bleached in droplets with a radius between 5 μM and 10 μM. Raw data were background subtracted and normalized using Excel and plotted using Graphpad Prism software. FRAP curves were fitted with a one phase exponential curve. Images were formatted using FIJI and ImageJ software.

Droplet fusion experiments

Samples with fluorescent droplets were incubated in plastic Cell Counter slides (Bio-Rad) at room temperature and immediately imaged on a Zeiss LSM 780 Meta NLO confocal microscope equipped with a 20x long-range objective. Time-lapse images were taken of droplets settling on the cover slip and fusing together. Fusion events were manually identified and measured using FIJI and ImageJ software. Relaxation curves were plotted using Graphpad Prism software and fitted with one-phase exponential decay curves. Relaxation times (τ) were calculated by Graphpad prism and used for estimating the inverse capillary velocity (η/γ) via following formula: $\tau \approx (\eta/\gamma)L$ where L is the characteristic length scale of the droplet, as described in (4, 5).

Partitioning analysis

Fluorescent droplets were incubated in plastic Cell Counter slides (Bio-Rad) at room temperature. Chambers were sealed using nail varnish to prevent evaporation during aging. Random fields of view were obtained on a Zeiss LSM 780 Meta NLO confocal microscope equipped with a 20x long-range objective. Ratio of fluorescence intensity in the droplets over the surrounding background was calculated for individual droplets using Excel and plotted using Graphpad Prism software.

Statistical analysis

All statistical and regression analyses were carried out using Graphpad Prism. Details are indicated in the figure legends. * p-value: 0.01-0.05, ** p-value: 0.01-0.001, *** p-value: 0.001-0.0001, **** p-value < 0.0001.

Soft x-ray tomography (SXT)

After induction of phase separation, the droplets were loaded in thin-wall glass capillaries and rapidly frozen in liquid propane, for details see previous work (6, 7). The specimens were imaged by XM-2, a soft x-ray microscope in the National Center for X-ray tomography (hhtp://ncxt.lbl.gov) located at the Advanced Light Source of Lawrence Berkeley National Laboratory. The x-ray microscope operates at the "water-window" region of soft x-rays, providing natural contrast of biomolecules with respect to water. The condenser, objective lens and magnification, chosen for this experiment, guaranteed isotropic 32 nm voxel size. For 3D reconstructions, 92 projection images, with 200 ms exposure time each, were acquired sequentially around a rotation axis with 2° increment angles. After normalization and alignment, tomographic reconstructions were calculated using iterative reconstruction methods. The segmentation and visualization of multilayered condensates was performed using linear attenuation coefficient of x-rays (8) in Amira 6.3.0.

Coarse-grained simulations

All simulations were performed using coarse-grained lattice-based models. The simulations themselves deploy Monte Carlo sampling and the brand of models deployed here has been used previously to study phase behavior (9-11). The model is based on a standard granular lattice mode in which each bead occupies a single site on the lattice, which defines the excluded volume per bead. Any given bead interacts with every adjacent lattice site and engages via bead-bead and bead-solvent interactions, where empty lattice sites are taken to be occupied by solvent. Each simulation involves more than 10^9 independent moves. Finite size artifacts were overcome by including at least 2×10^4 particles. The cubic lattices have dimensions of 80^3 or 100^3 depending on the simulation in question. Five independent simulations where run, for each simulation type, and we find extremely good agreement across independent simulation runs (**Figure S3**). Two different types of simulations were run: One set examined the formation of arrested network assemblies (**Figure 2**), and the second set examined equilibrium droplet topology associated with multicomponent droplets (**Figure 5**).

For simulations used to examine the formation of arrested network assemblies, we followed the formalism of Dynamic Monte Carlo (DMC) (12-15). In DMC, two classes of moves are performed, moves that locally perturb each bead or particle according to some limited distance that corresponds to the distance moved by the particle over some characteristic time-step, and rigid body moves that rotate or translate individual or clusters of molecules according to their molecular mass. In our implementation, we only perform the first set of moves. This leads to a slowdown in the absolute convergence times; however, the simulations are fast enough that this is of minimal practical impact. However, it also avoids the potentially misleading impact of translating species of vastly different sizes in a manner that considers only mass and not the effective hydrodynamic drag. This becomes important because $(PR)_{30}$ and polynucleotides are of dramatically different molecular weights and contour lengths (see below). Importantly, assuming we are comparing two simulations with an identical distribution of species, we are able to formally assess relative changes in relaxation and equilibration.

For the simulations performed to examine multilayered topologies, we focused on equilibrium properties. With this in mind, in addition to the local moveset described above, we allow an additional set of Monte Carlo moves (translation, rotation, cluster translation and rotation, chain pivot) which improves sampling. In all cases, our movesets preserve detailed balance. We define arrested network assemblies as those in which the simulation reaches a state that is exponentially stable, yet demonstrably higher in energy than another configuration that can be reached via heating and cooling (simulated annealing) (**Figure S3**). In all systems, $(PR)_{30}$ and polyN (poly-rA, poly-rC, or poly-rU) are represented explicitly. The ratio of contour lengths between $(PR)_{30}$ (~300 Å) and polyN of around 600 kDa RNA (~10 000 Å) is around 1:30. Consequently, we represent each $(PR)_{30}$ molecule as a single multivalent bead, while each RNA molecule consists of 30 beads. Each bead is able to engage in up to 26 interactions (every face/diagonal of a cube) in the lattice. Relative contour lengths for RNA and protein are based on a nucleotide/amino acid contour length of 5 Å and 3.6 Å, respectively. While these are clearly order-of-magnitude simplifications, varying length distributions (within the associated order of magnitude) had no material effect on results (**Figure S10**). The simulations performed represent a minimal coarse-grained model that is able to recapitulate the observed behavior. There is nothing in the model that reflects the fact that the polymers are RNA and protein, as opposed to generic polymers with specific preferential interactions. It is almost inconceivable that for naturally occurring RNA there will not be significant additional complexity associated with protein-RNA interactions. Moreover, we make no attempt to consider the impact of solution conditions.

However, for a simple homopolymeric system we seem able to capture many of the macroscopically observable features with simple intuitive models. Simulation trajectories were analyzed using locally written code using filesystem operations implemented in MDTraj (16), while simulation snapshots were generated using VMD (17).

Supporting Figures

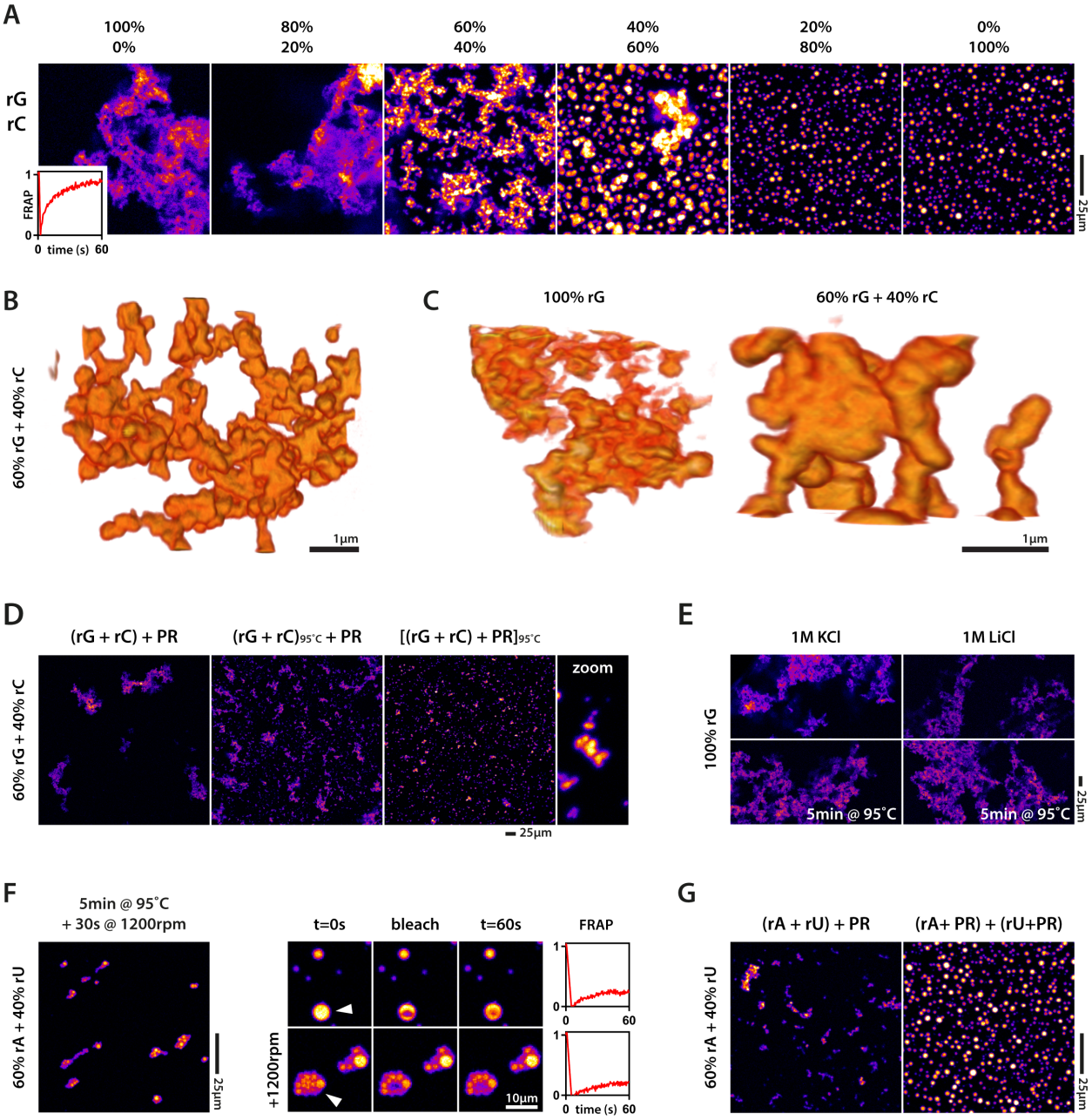

Fig. S1: Supplemental material related to Figure 2. (A) G:C base pairing disrupts large poly-rG-PR networks. (B) 3D model of poly-rG:rC-PR networks as visualized by soft x-ray tomography. (C) Comparison between poly-rG-PR and poly-rG:rC-PR networks. (D) Boiling disrupts large poly-rG:rC-PR networks, but does not results in spherical liquid-like assemblies. (E) poly-rG-PR networks withstand disruption even when boiled in high concentrations of Li^{+} (F) Boiled poly-rA:rU-PR coacervates fail to fuse upon centrifugation and retain PR dynamics. (G) poly-rA:U base pairing results in filamentous network formation upon coacervation, whereas initial PR addition prevents open network formation.

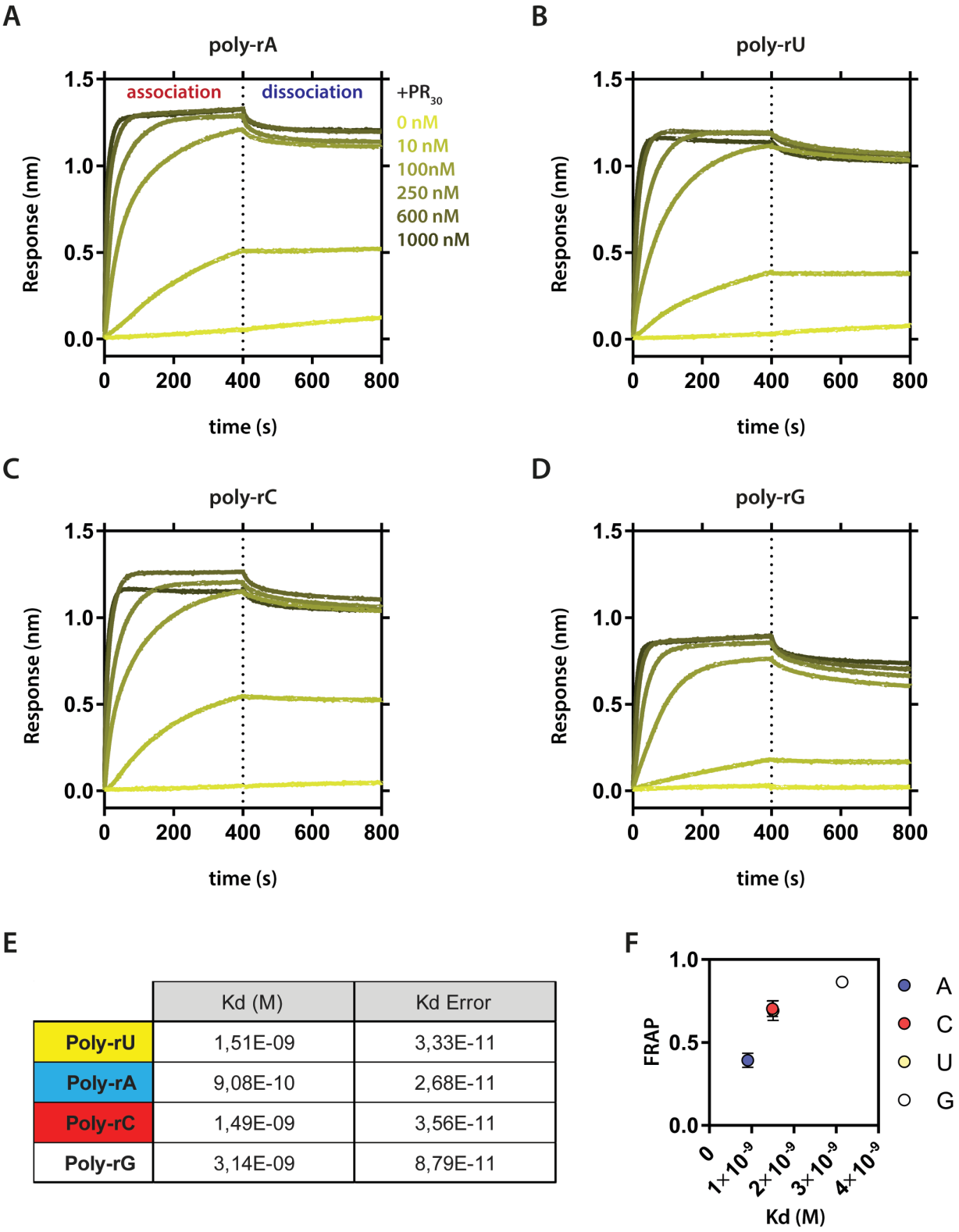

	Kd (M)	Kd Error
Poly-rU	1,51E-09	3,33E-11
Poly-rA	9,08E-10	2,68E-11
Poly-rC	1,49E-09	3,56E-11
Poly-rG	3,14E-09	8,79E-11

Fig. S2: Supplemental material related to Figure 3. (A-D) Interferograms of PR_{30} association and dissociation to homopolymeric RNA recorded on an Octet RED96 bio-layer interferometer. (A) poly-rA, (B) poly-rU, (C) poly-rC and (D) poly-rG. (E) Table summarizing K_d values

calculated based on 600nM curves. (F) K_d correlates with FRAP dynamics. Of note, since poly-rG coacervates have a different morphology compared to the other coacervates (i.e., sparse networks versus dense liquid droplets) we cannot rule out that at least part of the differences in FRAP dynamics are because of differences relating to diffusion characteristics in such vastly different structures.

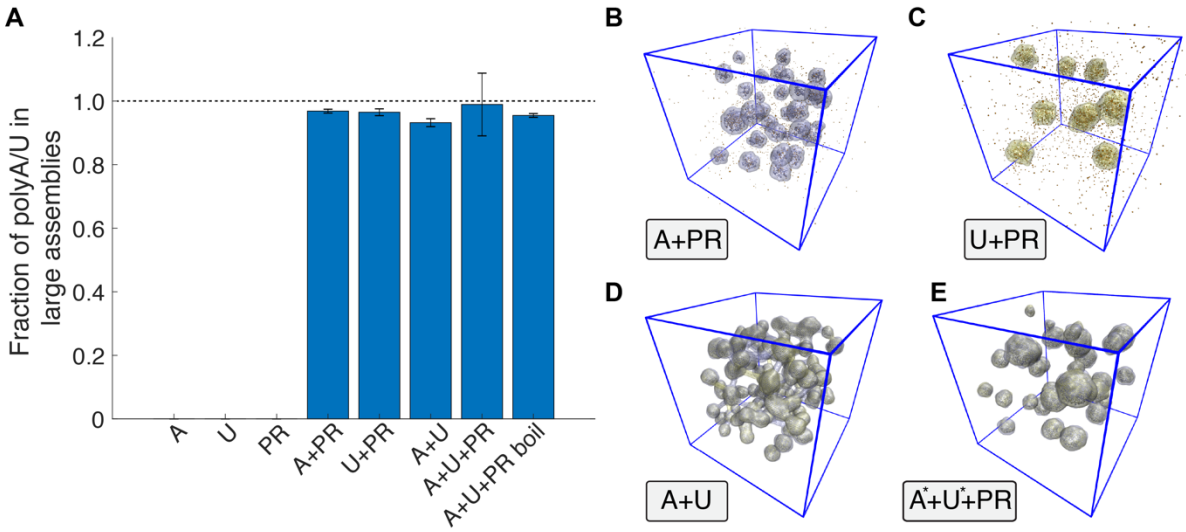

Fig. S3: Simulations reproduce morphology observed *in vitro*. (A) The fraction of poly-rA or poly-rU in large assemblies (10 or more poly-rA/U species in a connected cluster) was assessed for poly-rA alone, poly-rU alone, PR alone, poly-rA+PR, poly-rU+PR, poly-rA+poly-rU, poly-rA+poly-rU+PR before boiling, and poly-rA+poly-rU+PR after boiling. We found that for all single component simulations no assemblies formed whatsoever. However, for all other combinations the overwhelming majority of poly-rA and/or poly-rU coalesced into large assemblies. Error bars are standard error of mean taken from five independent simulations (B) Poly-rA+PR forms dynamic spherical assemblies that undergo internal re-arrangement (see movie S4). (C) Identical behavior to poly-rA was observed for poly-rU. Note the difference in the number of spherical droplets reflects the stochastic merging of droplets. (D) poly-rA+poly-rU combined formed arrested extended networks that were highly similar to poly-rA+poly-rU in the presence of PR, further supporting the interpretation that network assembly depends on complementary base pairing. (E) Simulations were also run where the poly-rA-poly-rU pairwise interaction was reduced in strength to match that of the poly-rA/poly-rU-PR interaction strength. Under these conditions, while an open network initially forms, this re-arranges itself into a series of spherical droplets.

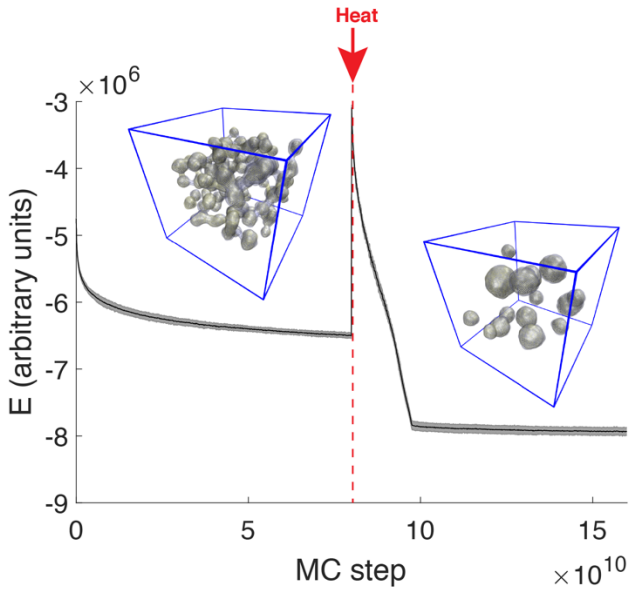

Fig. S4: Potential energy of simulations of poly-rA+poly-rU+PR before and after heating and cooling. Relaxation of potential energy as a function of the number of Monte Carlo steps. Prior to heating the potential energy relaxes to an approximate plateau that is undergoing very slow relaxation. After heating, upon network melting the potential energy jumps, and then during cooling rapidly decreases as poly-rA-poly-rU interactions form with preferred organization allowing for the formation of more favorable spherical assemblies that enhance the fraction of matched poly-rA:rU base pairs. Shaded area is potential energy standard deviation taken from five independent simulations. Movie S5 shows this process.

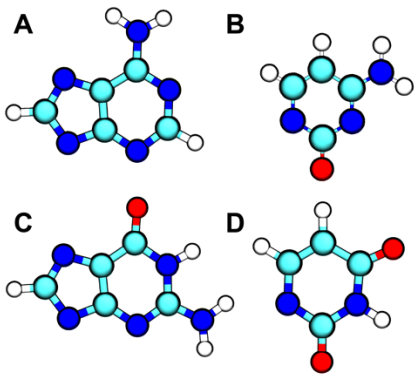

Fig. S5: Chemical structures of RNA nucleobases. (A) Adenine (rA), (B) Cytosine (rC), (C) Guanine (rG), and (D) Uracil (rU).

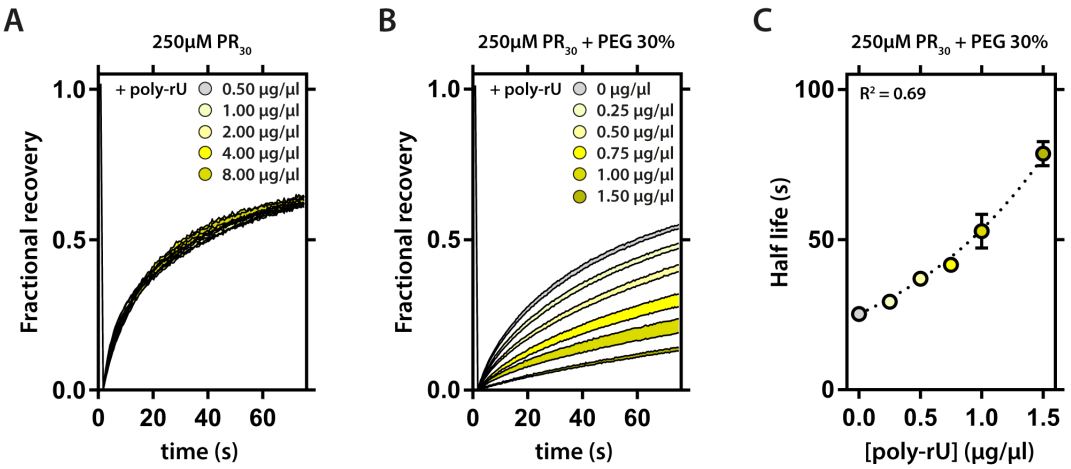

Fig. S6: RNA concentration tunes PR dynamics. (A) Increasing the concentration of poly-rU in a PR solution results in PR-RNA droplets with identical PR dynamics. Traces indicate SEM (B) Increasing the concentration of poly-rU in PEG-induced PR droplets decreases PR dynamics, even at lower RNA concentrations than used for PR-RNA droplet formation in the absence of PEG. Traces indicate SEM. (C) FRAP half-life correlates with RNA concentration. SD error bars, exponential growth equation fitted.

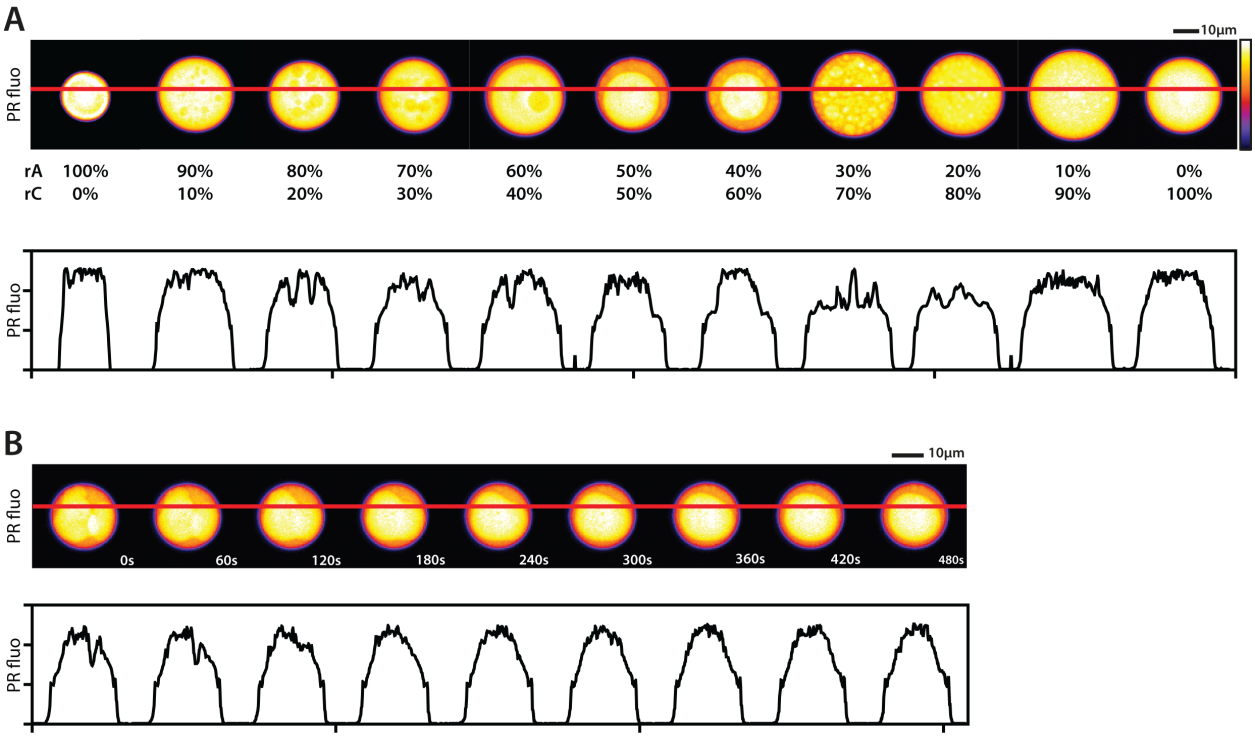

Fig. S7: Supplemental material related to Figure 4. (A) Line scan of PR fluorescence intensity over the different multidroplets shown in Figure 4A. (B) Line scan of PR fluorescence intensity over the fusion timecourse shown in Figure 4B.

>FUS$^{1\text{-}163}$ (UniProt ID: P35637)

MASNDYTQQA TQSYGAYPTQ PGQGYSQQSS QPYGQQSYSG YSQSTDTSGY
GQSSYSSYGQ SQNTGYGTQS TPQGYGSTGG YGSSQSSQSS YGQQSSYPGY
GQQPAPSSTS GSYGSSSQSS SYGQPQSGSY SQQPSYGGQQ QSYGQQQSYN
PPQGYGQQNQ YNS

>hnRNPA2$^{202\text{-}353}$ (Uniprot ID: P22626)

GRGGNFGFGD SRGGGGNFGP GPGSNFRGGS DGYGSGRGFG DGYNGYGGGP
GGGNFGGSPG YGGGRGGYGG GGPGYGNQGG GYGGGYDNYG GGNYGSGNYN
DFGNYNQQPS NYGPMKSGNF GGSRNMGGPY GGGNYGPGGS GGSGGYGGRS
RY

Fig. S8: Amino acid sequence of FUS and hnRNPA2 low complexity domains. Note FUS lacks any positively charged residues, while hnRNPA2 contains both aromatic (tyrosine, phenylalanine), and arginine residues.

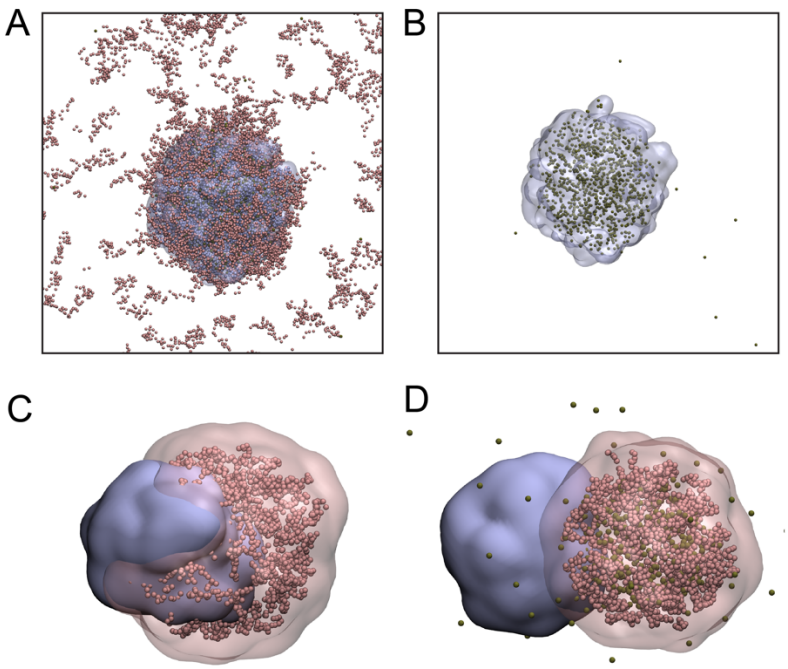

Fig. S9: Alternative multi-droplet topologies. (A) If poly-rA-PR interaction is stronger than poly-rC-PR interaction and the concentration of PR is low, any available PR is sequestered by poly-rA, inhibiting the formation of a poly-rC-PR droplet. Panel A highlights poly-rA (blue) and poly-rC (red) explicitly, with the enveloping surface around the poly-rA droplet also shown as a transparent shell. (B) shows the same snapshot as in A, but only the poly-rA droplet surface is shown along with PR. This illustrates the sequestration of PR into the poly-rA droplet. (C) The observed topology if poly-rA-poly-rA interactions are strong while poly-rA-poly-rC and poly-rC-poly-rC are equal in strength. There is no driving force to drive a core-shell architecture, and instead two discrete but touching and somewhat overlapping droplets form. (D) If poly-rA and poly-rC are repulsive for one another and share a common component (PR) two rounded, discrete, but apparently touching droplets form, where the interface between the two is mediated by a dynamic PR phase.

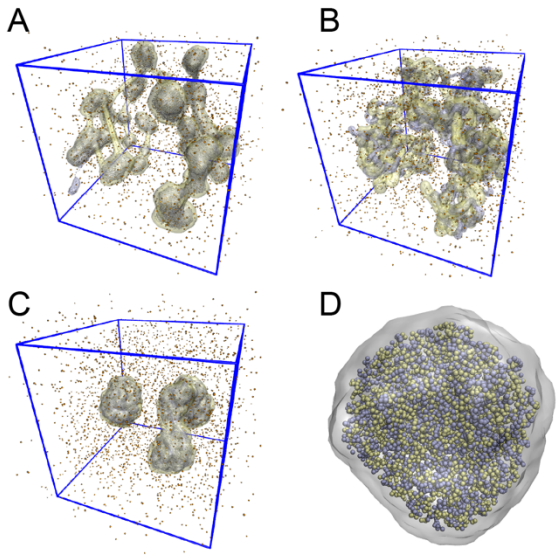

Fig. S10: Assessment of how RNA-polymer length influences poly-rA+poly-rU+PR simulation results. Our model assumes a 1:30 ratio of PR:RNA contour length. To assess how this influences our findings, we repeated simulations with a 1:240 contour length ratio and found qualitatively identical results. These simulations were performed with two different poly-rA-poly-rU interaction strengths, (the strength used in the 1:30 ratio simulations, and 0.5 that value) with identical results obtained. (A) Arrested network that forms before boiling. (B) Network melting immediately after boiling. (C) Spherical assembly formation. (D) Example of a single spherical assembly.

SUPPLEMENTAL MOVIES

Movie S1: 3D reconstructions of homopolymeric RNA-PR droplets and networks.

Movie S2: Comparison between poly-rG and poly-rG+poly-rC open networks.

Movie S3: 3D reconstruction of poly-rA+poly-rU+PR open networks.

Movie S4: Poly-rA+PR droplets are spherical and undergo internal re-arrangement. PR is not shown for clarity. Simulations are stopped after a finite length of time, leading to the formation of some number of spherical assemblies. However, given longer simulations all droplets would be expected to eventually fuse into a single spherical assembly. We cannot necessarily determine if the multiple droplets observed *in vitro* (see Figure 2A) reflect a kinetic effect as observed in these simulations, or a more complex size capping due to one or more equilibrium phenomena.

Movie S5: **Poly-rA+poly-rU+PR network melts and re-forms into spherical assemblies upon heating.** Note that unlike poly-rA+PR the spherical droplets that form stop undergoing internal re-arrangement, in agreement with the absence of RNA dynamics observed in Figure 3.

Movie S6: 3D reconstructions of free and wetting poly-rA+poly-rC+PR multi-layered condensates.

1. Burke KA, Janke AM, Rhine CL, & Fawzi NL (2015) Residue-by-Residue View of In Vitro FUS Granules that Bind the C-Terminal Domain of RNA Polymerase II. *Mol Cell* 60(2):231-241.
2. Ryan VH*, et al.* (2018) Mechanistic View of hnRNPA2 Low-Complexity Domain Structure, Interactions, and Phase Separation Altered by Mutation and Arginine Methylation. *Mol Cell* 69(3):465-479 e467.
3. Boeynaems S, De Decker M, Tompa P, & Van Den Bosch L (2017) Arginine-rich Peptides Can Actively Mediate Liquid-liquid Phase Separation. *Bio-protocol* 7(17).
4. Brangwynne CP, Mitchison TJ, & Hyman AA (2011) Active liquid-like behavior of nucleoli determines their size and shape in Xenopus laevis oocytes. *Proc Natl Acad Sci U S A* 108(11):4334-4339.
5. Brangwynne CP*, et al.* (2009) Germline P granules are liquid droplets that localize by controlled dissolution/condensation. *Science* 324(5935):1729-1732.
6. Le Gros MA*, et al.* (2011) Visualizing Sub-cellular Organization Using Soft X-ray Tomography. *Comprehensive Biophysics, Vol 2: Biophysical Techniques for Characterization of Cells*:90-110.
7. Le Gros MA*, et al.* (2014) Biological soft X-ray tomography on beamline 2.1 at the Advanced Light Source. *J Synchrotron Radiat* 21:1370-1377.
8. Le Gros MA*, et al.* (2016) Soft X-Ray Tomography Reveals Gradual Chromatin Compaction and Reorganization during Neurogenesis In Vivo. *Cell reports* 17(8):2125-2136.
9. Harmon TS, Holehouse AS, Rosen MK, & Pappu RV (2017) Intrinsically disordered linkers determine the interplay between phase separation and gelation in multivalent proteins. *eLife* 6.
10. Fei JY*, et al.* (2017) Quantitative analysis of multilayer organization of proteins and RNA in nuclear speckles at super resolution. *J Cell Sci* 130(24):4180-4192.

11. Feric M*, et al.* (2016) Coexisting liquid phases underlie nucleolar subcompartments. *Cell* 165(7):1686-1697.
12. Fichthorn KA & Weinberg WH (1991) Theoretical foundations of dynamical Monte Carlo simulations. *The Journal of chemical physics* 95(2):1090-1096.
13. Bieler NS, Knowles TP, Frenkel D, & Vácha R (2012) Connecting macroscopic observables and microscopic assembly events in amyloid formation using coarse grained simulations. *PLoS computational biology* 8(10):e1002692.
14. Šarić A*, et al.* (2016) Physical determinants of the self-replication of protein fibrils. *Nat. Phys.* 12(9):874-880.
15. Šarić A, Chebaro YC, Knowles TPJ, & Frenkel D (2014) Crucial role of nonspecific interactions in amyloid nucleation. *Proceedings of the National Academy of Sciences* 111(50):17869-17874.
16. McGibbon RT*, et al.* (2015) MDTraj: a modern, open library for the analysis of molecular dynamics trajectories. *Biophys. J.* 109(8):1528-1532.
17. Humphrey W, Dalke A, & Schulten K (1996) VMD: Visual molecular dynamics. *J. Mol. Graph. Model.* 14(1):33-38, 27-38.